

(Submitted to *International Journal of Heat and Mass Transfer*)

**EFFECTS OF MAGNETIC FIELDS ON G-JITTER INDUCED CONVECTION AND
SOLUTE STRIATION DURING SPACE PROCESSING OF SINGLE CRYSTALS**

K. Li and B. Q. Li*
School of Mechanical and Materials Engineering
Washington State University
Pullman, WA 99163

and

H. C. de Groh
NASA Lewis Research Center
Cleveland, OH 44135

February, 2002

This report is a preprint of an article submitted to a journal for publication. Because of changes that may be made before formal publication, this preprint is made available with the understanding that it will not be cited or reproduced without the permission of the author.

* To whom correspondence should be made.

ABSTRACT

A 2-D finite element model is presented for the melt growth of single crystals in a microgravity environment with a superimposed DC magnetic field. The model is developed based on the deforming finite element methodology and is capable of predicting the phenomena of the steady and transient convective flows, heat transfer, solute distribution, and solid-liquid interface morphology associated with the melt growth of single crystals in microgravity with and without an applied magnetic field. Numerical simulations were carried out for a wide range of parameters including idealized microgravity conditions, the synthesized g-jitter and the real g-jitter data taken by on-board accelerometers during space flights. The results reveal that the time varying g-jitter disturbances, although small in magnitude, cause an appreciable convective flow in the liquid pool, which in turn produces detrimental effects during the space processing of single crystal growth. An applied magnetic field of appropriate strength, superimposed on microgravity, can be very effective in suppressing the deleterious effects resulting from the g-jitter disturbances.

NOMEMCLATURE

\vec{U} : velocity vector
 u : x direction velocity component
 v : y direction velocity component
 p : pressure
 T : temperature
 C : concentration
 T_{m0} : melting temperature of pure Sn
 ρ_0 : density of pure Sn at T_m
 C_p : specific heat of Sn
 ν : kinematic viscosity
 D : solute diffusivity
 β_T : thermal expansion coefficient
 β_C : solutal expansion coefficient
 k_0 : segregation coefficient
 m : slope of solidus curve
 g_0 : earth gravity constant
 H : latent heat of Sn
 k : thermal conductivity
 κ : thermal diffusivity
 ε_{amp} : black body coefficient of ampoule
 W_i : inner width of ampoule
 W_o : outer width of ampoule
 L : length of three zones
 L_h : length of hot zone
 L_c : length of cold zone
 L_g : length of gradient zone
 dT/dx : temperature gradient
 T_h : hot zone temperature
 T_c : cold zone temperature
 V_g : crystal pulling speed
 B_0 : magnetic field magnitude
 U_0 : velocity scale
 ΔT : temperature scale
 R_0 : length scale
 t_0 : time scale

C_0 : concentration scale
 $h(y)$: dimensionless x - position of growth interface
 L_0 : dimensionless x - position of hot end
 L_1, L_4 : dimensionless lower and upper y - positions of ampoule outer surface
 L_2, L_3 : dimensionless lower and upper y - position of ampoule inner surface
 Pr : Prandtl number
 Sc : Schmidt number
 Gr_T : thermal Grashof number
 Gr_S : solutal Grashof number
 Ste : Stefan number
 Ha : Hartmann number
 Ra : radiation number of ampoule
 T_m : dimensionless melting point
 V_p : dimensionless pulling speed
 \vec{U}^* : interface velocity
 \hat{n} : unit normal vector
 \hat{i}, \hat{j} : unit vector of i th, j th component
 ε : penalty parameter for pressure
 Ω : computational domain
 $\partial\Omega$: computational domain boundary

Subscripts

cry : crystal
 amp : ampoule
 amb : ambient
 i, j : i th, j th component

Superscripts

T : matrix transpose

1. INTRODUCTION

Space flight experiments on the melt growth of single crystals indicate that natural convection induced by gravity perturbation or g-jitter has a strong influence on the defect formation in the crystals. One of the important characteristics of g-jitter-induced convection is that it occurs randomly in both direction and time, which is attributed to the nature of the g-jitter forces. During normal space flights, a gravity level of $10^{-6} g_0$ is established. This dynamic weightlessness condition experienced by flight vehicles is prone to perturbations that stem from a variety of sources, which include the crew motions, mechanical vibrations (pumps, motors, excitations of natural frequencies of spacecraft structures), spacecraft maneuvers and attitude, atmospheric drag and the Earth's gravity gradient [1]. Detailed studies on g-jitter effects reveal that g-jitter induced convection in spacecraft is directly related to the magnitude and frequency of the gravity perturbation and to the alignment of the gravity field with respect to the growth direction or the direction of the temperature gradient [2-6]. Crystal growth experiments further indicate that a residual gravity of $10^{-5} g_0$ is sufficient to cause appreciable fluid motion in the liquid, thereby resulting in the quality of the crystals being unacceptable. The orientation of the gravity vector with respect to the temperature gradient also plays an important role in convective melt flows. The velocity attains a maximum when the gravity vector is perpendicular to the temperature gradients.

Numerous numerical simulations have been conducted to understand and estimate the adverse effects of time varying g-jitter [6-10]. Both 2D and 3D numerical models have been developed for this purpose [4,5,11]. These models have been used to study the effects associated with both idealized single- and multiple-frequency g-jitter modulations and real g-jitter data collected by accelerometer during actual flight experiments. These studies showed that the frequency, amplitude and spatial orientation of the residual gravity vector all play an important role in determining the convective flow behavior of the system. When the residual accelerations oscillate about the positive and negative of an axis, the orientation of this direction relative to the

density gradient determines whether a mean flow is generated in the system [12]. Sinusoidal accelerations induce an oscillating convective flow and composition oscillation in the liquid. The resulting velocity and composition fields oscillate with the same frequency of the affecting gravity field. Benjapiyaporn *et al.* [13] reported a study on the g-jitter influence of solute transport and convection together with solidification in a planned space flight experiment configuration. They used the finite difference approximation for field calculations and the enthalpy method to model the solid-liquid interface. In their calculations, the melting temperature of the pure solvent was used to determine the solid-liquid interface. While the enthalpy method is very useful for alloy solidification with a distinctive mushy zone, it is in general considered inadequate for precisely capturing the solidification front of pure or nearly pure materials. They used simulated g-jitter data for their simulations to show that for large frequencies, the higher amplitude of the gravitational acceleration is required to produce effects on the segregation. Their study further illustrates that the concentration varies appreciable along the solid-liquid interface, suggesting that it is necessary to take into consideration the effects of concentration on the melting temperature to get an accurate estimate of the interface shape.

The use of the magnetic field to control the melt motion during single crystal growth has been widespread in the semiconductor industry. Because the magnetic damping effect comes from a different origin from that of gravity reduction, it is plausible to suppress the g-jitter effects by imposing an appropriate magnetic field [14]. Studies on the g-jitter-induced melt flows in the systems of relevance to space crystal growth experiments have been reported by Ma and Walker [12] and Baumgartl and Muller [11, 15]. The former presented a semi-analytical model for the magnetic field effects on g-jitter driven thermal convection, while the latter presented a 3-D model of melt flow driven by a single frequency g-jitter force parallel to the thermal gradient with either transverse or axial fields imposed. Recently, Li and his co-workers [7,14,16-20] have reported a series of studies, including both analytical analyses and numerical simulations, on the magnetic field effects on the g-jitter induced flows and mass transfer. Unlike others, their studies used both simulated g-jitter signatures and real g-jitter data taken from typical space flights, with the latter intended to obtain an understanding of the thermal and flow phenomena in a realistic g-jitter environment. In space vehicles, g-jitter is not aligned perfectly with the thermal gradient during crystal growth. The most deleterious flow effects, however,

result from the g-jitter component that is perpendicular to the thermal gradient [4]. The melt flow in microgravity is shown to have a very strong effect on the solute transport. Their studies further demonstrate that these deleterious g-jitter effects can be suppressed by the application of an external magnetic field. Thus far, these studies have been primarily concerned about the convection with or without solute striation in the presence of magnetic fields in the melt pool for a configuration, which is a version idealized, though relevant, version of a melt growth experiment furnace used for space flights. None of these studies have considered the solidification behavior, which is a critical part of the process. Nonetheless, these studies have provided a useful basis upon which models incorporating more realistic issues such as solidification and ampoule configuration, coupled with more realistic thermal boundary conditions. These more realistic models will provide a much more powerful tool not only for enhancing our fundamental understanding of fluid mechanics and thermal phenomena in space crystal growth systems but also for developing rational guidelines for both space experiment design and interpretation of experimental measurements.

In the present study, a finite element model is presented for the heat and mass transfer and solidification phenomena associated with the melt growth of single crystals in microgravity with and without an imposed magnetic field. The analysis is based on a 2-D geometry. It is noted that a furnace for the melt growth is of cylindrical geometry and under terrestrial conditions a 2-D axisymmetric condition can be established and maintained for field variables of interest [21]. In a microgravity environment, however, such an axisymmetry condition can not be maintained because the frequent maneuvering of space vehicles changes the gravity orientation constantly. It is also realized that because of the frequent change in gravity directions, in particular during the period when g-jitter sets in, the flow structure is truly three-dimensional and 3-D models should be developed to fully appreciate the complex 3-D flow structure [21]. Nonetheless, a 2-D analysis will provide some essential features of g-jitter induced flows and solidification behavior and thus form the required basis upon which 3-D models can be further developed. The 2-D analysis presented below is based on the solution of the Navier-Stokes equations for fluid flow, the energy balance equation for the temperature distribution and the mass balance equation for species transport in an Sn-doped Bi alloy melt. The numerical scheme entails the implementation of a quasi-Lagrangian deforming finite element approach where the solid-liquid

interface is tracked precisely by deforming the elements associated with the moving interface. This interface track approach allows us to accurately predict the interface shape change as a function of solute distribution, which is critical for space experiments but has not yet fully appreciated. Numerical simulations are conducted of the transient convective flows and solute redistribution in the melts and their effects on the solidification interface morphology under the combined action of g-jitter and external magnetic fields. Both synthetic g-jitter, which represents a single component of Fourier synthesis of g-jitter data, and the real g-jitter data are used in the analyses.

2. PROBLEM STATEMENT

Figure 1 schematically illustrates the 2-D model used to study the Bridgman-Stockbarger Sn-doped Bi single crystal growth in microgravity. An external DC magnetic field is applied along the thermal gradient. The ambient temperature profile (T_{amb}) consists a cold zone (T_c), a linear gradient zone (dT/dx) and a hot zone (T_h). In the present study, the pseudo-steady-state model (PSSM) [22] is adopted in which the translation of the ampoule is simulated by feeding the melt with the uniform impurity concentration C_0 into the inlet at the constant growth velocity V_g , while the crystal is withdrawn from the outlet at the speed that conserves the mass of the system. The length of the computation domain is L , the inner width of the ampoule is W_i and the outer width is W_o . The configuration described above is similar to that used for the MEPHISTO-2 and MEPHISTO-4 Space Flight experiments [6,23].

The residual acceleration experienced by the spacecraft in microgravity is composed of a steady acceleration component and a time-dependent acceleration component (g-jitter). The amplitude of the time-dependent component is much greater than that of the steady component. The real g-jitter data taken during space flight show that g-jitter changes both spatially and temporally. In some cases, to help analyses, g-jitter can be represented by the combination of a series of single frequency accelerations as follow:

$$\bar{g}(t) = \sum_{n=1}^N \bar{g}_n \sin(2\pi\omega_n t) \quad (1)$$

where \bar{g}_n is the amplitude and ω_n the frequency associated with the n th component of g-jitter. Both the synthetic and real g-jitter data are considered in the present study.

The time dependent phenomena of fluid flow, heat and mass transfer in the above system with the presence of an external magnetic field are described by the Navier-Stokes equations with the time varying gravity force and the Lorentz force resulting from the imposition of a magnetic field. For the melt flow, the standard Boussinesq approximation, $\rho = \rho_0[1 - \beta_T(T - T_{m0}) - \beta_C(C - C_0)]$, has been used. Furthermore, the thermoelectric effect, i.e., $\bar{J} = -S\nabla T$, is neglected, because of the lack of reliable data for the absolute thermoelectric power S of the fluid and also because it generates a flow component in the z -direction and thus violates the 2-D assumption. With an appropriate choice of scales, the governing equations may be non-dimensionalized and are given below. For the melt, these equations become

$$\nabla \cdot \bar{U} = 0 \quad (2)$$

$$\frac{\partial \bar{U}}{\partial t} + \bar{U} \cdot \nabla \bar{U} = -\nabla p + \nabla^2 \bar{U} - [Gr_T(T - T_m) + Gr_S(C - 1)]\bar{g}(t) + Ha^2(\bar{U} \times \bar{B} \times \bar{B}) \quad (3)$$

$$\frac{\partial T}{\partial t} + \bar{U} \cdot \nabla T = \frac{1}{Pr} \nabla^2 T \quad (4)$$

$$\frac{\partial C}{\partial t} + \bar{U} \cdot \nabla C = \frac{1}{Sc} \nabla^2 C \quad (5)$$

For the crystal and the ampoule, where a bulk flow is superimposed because of the choice of the coordinate system, only heat transfer analysis is needed. The solute diffusion in crystal is also ignored. With these simplifications, the governing equations can be written as follows,

$$\frac{\partial T_{cry}}{\partial t} + Vp(\hat{e}_x \cdot \nabla T_{cry}) = \frac{\kappa_{cry}}{\kappa} \frac{1}{Pr} \nabla^2 T_{cry} \quad (6)$$

$$\frac{\partial T_{amp}}{\partial t} + Vp(\hat{e}_x \cdot \nabla T_{amp}) = \frac{\kappa_{amp}}{\kappa} \frac{1}{Pr} \nabla^2 T_{amp} \quad (7)$$

In deriving the above equations, the following scales are used: $R_0 = 0.5W_i$ for length, $U_0 = \nu/R_0$ for velocity, $t_0 = R_0^2/\nu$ for time, $p_0 = \rho_0 U_0^2$ for pressure, C_0 for concentration, g_0 for gravity, B_0 for magnetic field, $\Delta T = (T_h - T_c)$ for temperature while the temperature is non-dimensioned by $(T - T_c)/\Delta T$. The non-dimension parameters are defined as:

$$\begin{aligned} Gr_T &= \beta_T R_0^3 g_0 \Delta T / \nu^2, & Gr_S &= \beta_S R_0^3 g_0 C_0 / \nu^2, \\ Pr &= \nu / \kappa, & Sc &= \nu / D, & Ra &= \varepsilon_{amp} \sigma R_0 (\Delta T)^3 / k_{amp}, \\ V_p &= V_g / U_0, & Ste &= H / \Delta T C_p, & Ha &= B_0 R_0 \sqrt{\sigma_m / \rho_0 \nu}, \end{aligned}$$

The boundary conditions for the configuration considered are determined by the physical constraints and are detailed below.

$$T = 0, \quad \text{at } x = 0, \quad L_1 \leq y \leq L_4 \quad (8)$$

$$T = 1, \quad \text{at } x = L_0, \quad L_1 \leq y \leq L_4 \quad (9)$$

$$\hat{n} \cdot \nabla T = -Ra \left[(T + T_c^*)^4 - (T_{amb} + T_c^*)^4 \right], \quad \text{at } 0 \leq x \leq L_0, \quad y = L_1 \text{ and } y = L_4 \quad (10)$$

$$\hat{n} \cdot \nabla T = (k_{amp} / k_{cry}) (\hat{n} \cdot \nabla T_{amp}), \quad \text{at } 0 \leq x \leq h(y), \quad y = L_2 \text{ and } y = L_3 \quad (11)$$

$$u = V_p, \quad v = 0, \quad \hat{n} \cdot \nabla C = 0, \quad \text{along the melt-ampoule interface} \quad (12)$$

$$\hat{n} \cdot \nabla T = (k_{amp} / k) (\hat{n} \cdot \nabla T_{amp}), \quad \text{at } h(y) \leq x \leq L_0, \quad y = L_2 \text{ and } y = L_3 \quad (13)$$

$$u = V_p, \quad v = 0, \quad \hat{n} \cdot \nabla C = V_p Sc (C - 1) (\hat{n} \cdot \hat{e}_x), \quad \text{at } x = L_0, \quad L_2 \leq y \leq L_3 \quad (14)$$

$$\hat{n} \cdot (\vec{l} - \vec{l}^*) = \hat{n} \cdot (\vec{l}_{cry} - \vec{l}^*), \quad \hat{n} \times (\vec{l} - \vec{l}_{cry}) = 0, \quad \text{at } x = h(y), \quad L_2 \leq y \leq L_3 \quad (15)$$

$$\hat{n} \cdot \nabla C = Sc \left[\hat{n} \cdot (\vec{U} - \vec{U}^*) C - \hat{n} \cdot (\vec{U}_{cry} - \vec{U}^*) C_{cry} \right], \quad \text{at } x = h(y), \quad L_2 \leq y \leq L_3 \quad (16)$$

$$T = T_m + mC, \quad \text{at } x = h(y), \quad L_2 \leq y \leq L_3 \quad (17)$$

$$(\hat{n} \cdot \nabla T) - (k_{cry} / k) (\hat{n} \cdot \nabla T_{cry}) = Ste Pr \hat{n} \cdot (\vec{U}_{cry} - \vec{U}^*), \quad \text{at } x = h(y), \quad L_2 \leq y \leq L_3 \quad (18)$$

where $T_c^* = T_c / \Delta T$, $C_{cry} = k_0 C$, $\hat{n} \cdot \vec{U}_{cry} = V_p$, $\hat{n} \times \vec{U}_{cry} = 0$.

3. THE FINITE ELEMENT SOLUTION

The governing equations described above along with the boundary conditions are solved using the deforming Galerkin finite element method. The stiffness matrix is obtained by using Galerkin's method of Weighted Residuals. The formulations and relevant benchmark tests were detailed in a series of papers published earlier [17, 24] and thus only a brief summary is given here. The governing equations are recast in an integral form and the field variables are interpolated using shape functions over the computational domain. With an appropriate algebraic manipulation, the following set of equations are obtained,

$$(\int_{\Omega} \hat{\psi} \cdot \nabla \phi^T dV) U_i = -\varepsilon (\int_{\Omega} \psi \psi^T dV) P \quad (19)$$

$$\begin{aligned} & (\int_{\Omega} \phi \phi^T dV) \frac{dU_i}{dt} + (\int_{\Omega} \phi \mathbf{u} \cdot \nabla \phi^T dV) U_i - (\int_{\Omega} \hat{\mathbf{i}} \cdot \nabla \phi \psi^T dV) P + (\int_{\Omega} \nabla \phi \cdot \nabla \phi^T dV) U_i \\ & + (\int_{\Omega} (\hat{\mathbf{i}} \cdot \nabla \phi) (\hat{\mathbf{j}} \cdot \nabla \phi^T) dV) U_j + (\int_{\Omega} \phi \theta^T \mathbf{g} dV) (\mathbf{T} - T_m) + (\int_{\Omega} \phi \theta^T \mathbf{g} dV) (\mathbf{C} - 1) \\ & = \int_{\partial\Omega} \mathbf{n} \cdot \boldsymbol{\tau} \cdot \hat{\mathbf{i}} \phi dS + \int_{\Omega} \phi H a^2 (\mathbf{u} \times \mathbf{B} \times \mathbf{B}) dV \end{aligned} \quad (20)$$

$$(\int_{\Omega} \text{Pr} \theta \theta^T dV) \frac{d\mathbf{T}}{dt} + (\int_{\Omega} \text{Pr} \theta \mathbf{u} \cdot \nabla \theta^T dV) \mathbf{T} + (\int_{\Omega} \nabla \theta \cdot \nabla \theta^T dV) \mathbf{T} = - \int_{\partial\Omega} q_T \theta dS \quad (21)$$

$$(\int_{\Omega} \text{Sc} \theta \theta^T dV) \frac{d\mathbf{C}}{dt} + (\int_{\Omega} \text{Sc} \theta \mathbf{u} \cdot \nabla \theta^T dV) \mathbf{C} + (\int_{\Omega} \nabla \theta \cdot \nabla \theta^T dV) \mathbf{C} = - \int_{\partial\Omega} q_c \theta ds \quad (22)$$

Once the form of shape functions ϕ , θ , and ψ for velocity, pressure and scalars are specified, the integrals defined in the above equations can be expressed in matrix form. Combining the momentum and energy equations into a single matrix equation gives rise to the following element stiffness matrix equation,

$$\begin{bmatrix} \mathbf{M} & 0 & 0 \\ 0 & \mathbf{N}_T & 0 \\ 0 & 0 & \mathbf{N}_C \end{bmatrix} \begin{bmatrix} \dot{\mathbf{U}} \\ \dot{\mathbf{T}} \\ \dot{\mathbf{C}} \end{bmatrix} + \begin{bmatrix} \mathbf{A}(\mathbf{U}) + \mathbf{K} + \frac{1}{\varepsilon} \mathbf{E} \mathbf{M}_p^{-1} \mathbf{E}^T & \mathbf{B}_T & \mathbf{B}_C \\ 0 & \mathbf{D}_T(\mathbf{U}) + \mathbf{L}_T & 0 \\ 0 & 0 & \mathbf{D}_C(\mathbf{U}) + \mathbf{L}_C \end{bmatrix} \begin{bmatrix} \mathbf{U} \\ \mathbf{T} \\ \mathbf{C} \end{bmatrix} = \begin{bmatrix} \mathbf{F} \\ \mathbf{G}_T \\ \mathbf{G}_C \end{bmatrix} \quad (23)$$

Note that in constructing the above element matrix equation, the penalty formulation has been applied, and \mathbf{P} in the momentum equation is substituted by $\frac{1}{\varepsilon} \mathbf{M}_p^{-1} \mathbf{E}^T \mathbf{U}$. The assembled global

matrix equations are stored in the skyline form and solved using the Gaussian elimination method. The coefficient matrices of Eq. (23) above are calculated by

$$\begin{aligned}
\mathbf{M}_p &= \int_{\Omega} \psi \psi^T dV; & \mathbf{N}_T &= \int_{\Omega} \text{Pr} \theta \theta^T dV \\
\mathbf{M} &= \int_{\Omega} \theta \theta^T dV; & \mathbf{N}_C &= \int_{\Omega} \text{Sc} \theta \theta^T dV \\
\mathbf{E}_i &= \int_{\Omega} \hat{i} \cdot \nabla \phi \psi^T dV; & \mathbf{L}_C &= \int_{\Omega} \nabla \theta \cdot \nabla \theta^T dV \\
\mathbf{L}_T &= \int_{\Omega} \nabla \theta \cdot \nabla \theta^T dV; & \mathbf{A}(\mathbf{U}) &= \int_{\Omega} \phi \mathbf{u} \cdot \nabla \theta^T dV \\
\mathbf{D}_C(\mathbf{U}) &= \int_{\Omega} \text{Sc} \theta \mathbf{u} \cdot \nabla \theta^T dV; & \mathbf{D}_T(\mathbf{U}) &= \int_{\Omega} \text{Pr} \theta \mathbf{u} \cdot \nabla \theta^T dV \\
\mathbf{B}_C &= \int_{\Omega} \text{Gr}_C (\mathbf{g} \phi \theta^T) dV; & \mathbf{B}_T &= \int_{\Omega} \text{Gr}_T (\mathbf{g} \phi \theta^T) dV \\
\mathbf{G}_C &= - \int_{\partial\Omega} q_C \theta dS; & \mathbf{G}_T &= - \int_{\partial\Omega} q_T \theta dS \\
\mathbf{F} &= \int_{\partial\Omega} \mathbf{n} \cdot \boldsymbol{\tau} \phi dS + \int_{\Omega} \phi \text{Ha}^2 (\mathbf{u} \times \mathbf{B} \times \mathbf{B}) dV + \int_{\Omega} \text{Gr}_C (\mathbf{g} \phi \theta^T) T_m dV + \int_{\Omega} \text{Gr}_T (\mathbf{g} \phi \theta^T) dV \\
\mathbf{K}_{ij} &= \left(\int_{\Omega} \nabla \phi \cdot \nabla \phi^T dV \right) \delta_{ij} + \int_{\Omega} (\hat{i} \cdot \nabla \phi) (\hat{j} \cdot \nabla \phi^T) dV
\end{aligned}$$

To implement the deforming finite elements to model the dynamic change of the moving interface, i.e., solidification front between the liquid and solid, a quasi-Lagrangian description is adopted. By this method, a region that covers the solidifying liquid and solid is defined and the nodes within the region are allowed to move in accordance with the interface movement. These additional velocities that result from the mesh movement are added to the velocity field as given in the above equations. The energy balance equation describing the latent heat release and interface change (Eq.18) is directly integrated within the context of weighted residuals,

$$\left(\int_{\Omega} \theta \hat{n} \cdot \nabla \theta^T dV \right) \mathbf{T} - \left(\int_{\Omega} (k_{\text{cry}}/k) \theta \hat{n} \cdot \nabla \theta^T dV \right) \mathbf{T}_{\text{cry}} = - \int_{\partial\Omega} q_T^* \theta dS \quad (24)$$

which is applied as a surface energy source to the total thermal energy balance equation, and added to the right-hand side of Eq. (23). Two basic algorithms have been applied in the past. One treats the moving interface as a separate variable and the interface thermal boundary condition in this present case would then be incorporated into the global finite element matrix.

The other treats the interface thermal boundary condition as a separate constraint and solved separately from the coupled field equations. Our numerical experience with these types of moving interface problems and solution algorithms shows that in a majority of cases the incorporation of the isothermal constraint into the global matrix results in a very unstable nonlinear system. The whole system is extremely sensitive to the boundary perturbations, more often than not, leading to divergence. Separation of the moving interface boundary coordinates from the global finite element solutions for field variables, however, requires the assurance of convergence of both moving interface coordinates and field variables in two related loops. For this case the global finite element matrix has a smaller bandwidth and thus requires a short CPU time for each iteration of field variable computations, which takes the majority of the computing time. Our tests further showed that the two methods require approximately the same CPU time, with the latter being much more robust and numerically stable. The latter has been used in the present study and for the results presented below. Also, there are two different methods used to track the liquid-solid interface and the results are the same within the machine accuracy. One method entails the use of the weighted residual method to integrate the interface thermal boundary condition (Eq. (17)), while the other the use of a directional search of the melting temperature after the coupled thermal, solute and fluid flow field calculations are converged. The latter is adopted in the present study.

In summary, our interface tracking strategy used in the present study involves an iterative procedure that entails applying the energy balance equation along the interface as a surface source and searching for the interface position coordinates based on each converged field calculations. The updated interface positions are the fed back to the field calculations until both the interface position coordinates and field variables are converged within a preset criterion, which is set at 1×10^{-4} for the results presented below.

4. RESULTS AND DISCUSSION

The finite element model described above permits the prediction of both steady and transient fluid flow, heat and mass transfer, along with the solid-liquid interface morphology in single crystal growth systems under both terrestrial and microgravity conditions with and without the presence of magnetic field in the axial direction. The model development was based on the finite

element code that has been reported in early studies, for example [7,14,16-20], which include both code development and benchmark testing. While both the formulations and computer code are general and can be applied to both 2-D and 3-D calculations, our focus here is on a 2-D simplification of a cylindrical system for growing binary single crystals in a microgravity environment. The thermo-physical properties and geometric dimensions for the study are given in Table 1. The studies used 2,968 9-node elements with the increasing mesh distribution near the interface. The penalty pressure formulation was used to approximate the pressure field. Tests were conducted to ensure the numerical results are mesh independent to within a tolerance of less 1% between two consecutively refined meshes. Numerical simulations were carried out for a wide range of conditions and a selection of the computed results is presented below.

1> Steady microgravity condition

Under an idealized microgravity condition, the gravity level is $10^{-6} g_0$. This condition may be obtained when the space vehicle follows the orbit perfectly without disturbances. Numerical simulations were carried out for this condition without an imposed magnetic field. The calculations will serve a dual purpose. The results are useful in helping to gain physical insight into the steady state behavior of the system. They also provide the initial condition for the dynamic behavior of the system when g-jitter effects set in. The simulations were based on the direct numerical solution to the steady state governing equations by dropping out the time dependent terms in the model equations described in Section 2 while keeping all the mutually coupled terms. For this case, the gravity is assumed to be oriented perpendicular to the growth direction, which represents the worst scenario case. The computed results show that the flow field is dominated overwhelmingly by the growth velocity, and the thermal and solutal gradient induced convective flow recirculation is small. These results are consistent with those obtained earlier from a simplified melt flow system where solidification was not considered [14], confirming that these simplified models indeed provide a good approximation to the melt flows under more realistic growth conditions, as they are intended to. Temperature distributions in the growth system are largely controlled by thermal conduction, which is a direct result of small Prandtl number for the system being studied. The solute distribution, on the other hand, appears to experience a slight distortion, which results from the small convection induced by the microgravity force.

Detailed analysis shows that for this case, the solute distribution has a striation of about 7%, measured by $(C_{\max} - C_{\min})/C_{\text{average}}$ along the solid-liquid interface. This concentration non-uniformity, according to Eq.(17), will affect the melting temperature and thus the system performance. Figure 2a compares the computed results of concentration and the normalized melting temperature distributions along the solid-liquid interface, and the solidification interface position for the system with and without taking into account the concentration effect on the melting temperature. Their differences are also showed in Figure 2b. It transpires that with the concentration effects considered, the melting temperature is no longer a constant, which results in a noticeable change in the solidification interface position. It is thus important to include the concentration effect on the melting temperature.

2> Single frequency g-jitter

Single frequency g-jitter represents an idealized perturbation to a microgravity environment. The Fourier analysis of g-jitter data collected by on-board accelerometers indicates that g-jitter has a wide range of frequency spectrum. However, space-flight experiments with single crystal growth suggest that only the low frequency g-jitter produces deleterious effects on the quality of the crystals. A single component g-jitter force provides a valuable means for developing a fundamental understanding of physics governing the effects of gravity perturbation on convection and solidification phenomena associated with space melt growth of crystals. The computed results for the dynamic development of fluid field, temperature and solute distribution and solidification interface morphology are given in Figures 3 to 4 for a quasi-steady state time harmonic cycle. The results were obtained a single frequency g-jitter, $g(t) = 10^{-3} g_0 \sin(0.2\pi t)$, oriented in the direction perpendicular to the thermal gradient without an imposed magnetic field. For this case, a strong convection recirculation develops in the melt pool, which covers the entire pool region. The convection loop oscillates and reverses its rotating direction with time at approximately the same frequency as the applied g-jitter. A very strong flow sweeps along the solid-liquid interface. Note that the ampoule and the solid move at the crystal pulling velocity with respect to the chosen frame of reference, in contrast to the recirculating convective flow motion in the liquid (see Figure 3). The effect of the convection on the concentration distribution in the melt is shown in Figure 4, where an appreciable concentration striation is

5. CONCLUDING REMARKS

This paper has presented a 2-D finite element model for the melt growth of single crystals in a microgravity environment with a superimposed magnetic field. The model is developed based on the deforming finite element methodology and is capable of predicting the phenomena of steady state and transient melt convective flows, heat transfer and solute distribution, and solid-liquid interface morphology associated with single crystal growth in microgravity with and without an applied magnetic field. The field variables are solved in a completely coupled fashion, with allowance made for the effects of solute striation on the melting temperature. Numerical simulations were carried out for a wide range of parameters including the idealized microgravity condition, the synthesized g-jitter and also real g-jitter data taken by on-board accelerometers during a space flight. The results show that the time varying g-jitter disturbances, although small in magnitude, indeed cause an appreciable convective flow in the liquid pool, which in turn produces detrimental effects during space growth of single crystals. An applied magnetic field of appropriate strength, superimposed on microgravity, can provide a viable means to suppress or eliminate (i.e. suppress beyond detection) the deleterious effects resulting from the g-jitter disturbance.

6. ACKNOWLEDGEMENT

The authors are grateful for the financial support of this work by the NASA Microgravity Science and Application Division (Grant No.: NAG8-1693).

REFERENCES

- [1] B. N. Antar and V. S. Nuotio-Antar, Fundamentals of low gravity fluid dynamics and heat transfer, CRC Press, Boca Ration, FL (1993).
- [2] H. C. De Groh III and E. S. Nelson, On residual acceleration during space experiments. ASME winter annual meeting, Chicago, Nov 6-11, HTD-Vol. 290 (1994), pp. 23-33.
- [3] S. Schneider and J. Straub, Influence of the Prandtl number on laminar natural convection in a cylinder caused by g-jitter. J. Crystal Growth, Vol. 97 (1989), pp. 235-242,
- [4] J. I. D. Alexander, S.Amiroudine, J. Quazzani and F. Rosenberger, Analysis of the low gravity tolerance of the Bridgman-Stockbarger crystal growth II: transient and periodic accelerations, J. Crystal Growth, Vol. 113(1991), pp. 21-38.
- [5] J. I. D. Alexander, J. Quazzani and F. Rosenberger, Analysis of the low gravity tolerance of the Bridgman-Stockbarger crystal growth I: Steady and impulse accelerations, J. Crystal Growth, Vol. 97 (1989), pp. 285-302.
- [6] E. S. Nelson, An examination of anticipated g-jitter in space station and its effects on materials processes, NASA TM 103775 (1991).
- [7] B. Q. Li, Stability of modulated-gravity-induced thermal convection in magnetic fields, Physical Review E, Vol. 63 (2001), pp. 416-514.
- [8] W. Zhang, J. Casademunt and J. Venals, Study of parametric oscillator driven by narrow-band noise to model the response of a fluid surface to time-dependent acceleration, J. Phys. Fluids A, Vol. 5(1993), pp. 3147-3152.
- [9] A. A. Wheeler, G.B. Mcfadden, B.T. Murray and S.R. Coriell, Convection stability in Rayleigh-benard and directional solidification problems: high frequency gravity modulation. J. Phys. Fluids A, Vol. 3 (1991), pp. 2847-2853.
- [10] J. I. D. Alexander, Low-gravity experiment sensitivity to residual acceleration: a review, Microgravity Sci. Tech., Vol. 2 (1994), pp. 131-135.
- [11] J. Baumgartl, M. Gewald, R. Rupp, J.Stierlen and G. Muller, in Proc. of VIth Euro. Symp. on Materials and Fluids Sciences in Microgravity, Oxford, UK (1990), pp. 47-52.
- [12] N. Ma and J. S. Walker, Magnetic damping of buoyant convection during semiconductor crystal growth in microgravity: Spikes on residual acceleration, Physics of Fluids, Vol. 8 (4) (1996), pp. 944-949.

- [13] C. Benjapitayorn, V. Timchenko, E. Leonardi, G. De Vahl Davis and H. C. De Groh III . Effects of space environment on flow and concentration during directional solidification, NASA TM 209293(2000).
- [14] B. Pan, D. Y. Shang, B.Q. Li and H. C. De Groh III, Magnetic damping effects on g-jitter driven melt convection and mass transfer in microgravity, *Inter. J. Heat & Mass transfer*, Vol. 45(2002), pp. 125-144.
- [15] J. Baumgartl and G. Muller, The use of magnetic fields for damping the action of gravity fluctuations (g-jitter) during crystal growth under microgravity. *J. Crystal Growth* 169(1996) 582-586.
- [16] D. Y. Shang, B.Q. Li and H. C. De Groh III, Magnetic damping of g-jitter driven flows:3-D calculations, *J. Jpn. Soc. Microgravity Appl.* Vol. 15, Supplement II (1998), pp. 108-113.
- [17] B. Pan and B. Q. Li, Effects of magnetic field on oscillating mixed convection. *Int. J. Heat Mass Trans.*, Vol. 41 (1998), pp. 2705-2710.
- [18] B. Q. Li, Stability of modulated-gravity-induced thermal convection in a magnetic field, *Physical Review E*, Vol. 63, (2001), pp. 041508-1-041508-9.
- [19] Y. Shu, B. Q. Li and H. C. de Groh, Magnetic damping of g-jitter induced double diffusive convection in microgravity, *Numerical Heat Transfer A: Application*, accepted.
- [20] B. Q. Li and R. He, "Computational modeling of electrodynamic and transport phenomena under terrestrial and microgravity conditions," *Int. J. of Applied Electromagnetics & Mech.*, in printing.
- [21] J. Honda, C. Zhang, B. Q. Li and H. C. de Groh, "A 3-d model for magnetic damping of g-jitter induced convection and solutal transport in a simplified Bridgmann configuration," in the *Proceedings of the ASME Heat Transfer Division*, New York, NY, Nov. 2001.
- [22] D.H. Kim, P.M. Adornato and R. Brown, Effect of Vertical Magnetic Field on Convection and Segregation in Vertical Bridgman Crystal Growth, *J. Crystal Growth*, Vol. 89(1988) pp. 339-356.
- [23] K. Morgan, R.W. Lewis and O.C. Zienkiewicz, an Improved Algorithm for Heat Conduction Problems with Phase Changes, *Int. J. Numer. Meth. Eng.*, Vol. 12(1978) pp.1191-1195.

- [24] S.P. Song and B.Q. Li, Surface Deformation and Marangoni Flow in Electrostatically Levitated Droplets. *Int. J. Heat Mass Transfer*, Vol. 43(2000), pp. 3589-3606.
- [25] S. P. Song and B. Q. Li, A hybrid boundary/finite element method for simulating viscous flows and shapes of droplets in electric fields, *Int. J. Comp. Fluid Dyn.*, Vol. 15, pp. 293-308.

Table 1. Parameters used for calculations

Physics properties		L_h	$4.95 \times 10^{-3} \text{ m}$
T_{m0}	544 K	L_c	$4.95 \times 10^{-3} \text{ m}$
ρ_0	10070 kg m^{-3}	L_g	$3.21 \times 10^{-3} \text{ m}$
C_p	$144.87 \text{ J kg}^{-1} \text{ K}^{-1}$	dT/dx	$2.0 \times 10^4 \text{ Km}^{-1}$
ν	$1.837 \times 10^{-7} \text{ m}^2 \text{ s}^{-1}$	T_h	973 K
D	$2.7 \times 10^{-9} \text{ m}^2 \text{ s}^{-1}$	T_c	323 K
C_0	1 at%	V_g	$-3.34 \times 10^{-6} \text{ ms}^{-1}$
β_T	$1.25 \times 10^{-4} \text{ K}^{-1}$	B_0	0.5 T
β_C	$-0.3049 \text{ (volume fraction)}^{-1}$	Scale parameters	
k_0	0.29 at\%/at\%	U_0	$6.12 \times 10^{-5} \text{ ms}^{-1}$
m	2.32 K/at\%	ΔT	650 K
g_0	9.8 ms^{-2}	R_0	$3 \times 10^{-3} \text{ m}$
H	$5.25 \times 10^4 \text{ J kg}^{-1}$	t_0	49.0 s
k	$12.4 \text{ Wm}^{-1} \text{ K}^{-1}$	Nondimensional parameters	
k_{cry}	$6.5 \text{ Wm}^{-1} \text{ K}^{-1}$	Pr	0.0215
k_{amp}	$2.01 \text{ Wm}^{-1} \text{ K}^{-1}$	Sc	68.0
κ	$8.5 \times 10^{-6} \text{ m}^2 \text{ s}^{-1}$	Gr_T	6.37×10^5
κ_{cry}	$4.5 \times 10^{-6} \text{ m}^2 \text{ s}^{-1}$	Gr_S	-1.957×10^4
κ_{amp}	$8.7 \times 10^{-7} \text{ m}^2 \text{ s}^{-1}$	Ste	0.558
ε_{amp}	0.8	Ha	38.7
System parameters		Ra	0.01859
W_i	$6.0 \times 10^{-3} \text{ m}$	T_m	0.34
W_o	$1.0 \times 10^{-2} \text{ m}$	V_p	-0.055
L	$4.2 \times 10^{-2} \text{ m}$	T_c^*	0.497

Figure Captions

Figure1. Schematic representation of the 2-D model for the Bridgman-Stockbarger Sn-doped Bi single crystal growth system in microgravity.

Figure2. Dependency of interface position on concentration striation along the interface: (a) the interface positions, the temperature and concentration distributions along the growth interface of the steady cases with and without concentration effect respectively and (b) their differences.

Figure3. The development of the flow field caused by a single frequency g-jitter in one time harmonic cycle in the absence of magnetic field: (a) $t = 3.876$, $U_{\max} = 0.6161$
(b) $t = 3.927$, $U_{\max} = 0.6922$ (c) $t = 3.978$, $U_{\max} = 0.6161$ (d) $t = 4.029$, $U_{\max} = 0.6920$.

Figure4. The development of the concentration distribution caused by a single frequency g-jitter in one time harmonic cycle in the absence of magnetic field: (a) $t = 3.876$ (b) $t = 3.927$ (c) $t = 3.978$ (d) $t = 4.029$. From left to right, $C_{\max} = 3.52$ reduced to $C = 1.06$, $\Delta C = 0.35$

Figure5. The development of (a) the interface positions, (b) the temperature and (c) concentration distributions along the growth interface caused by a single frequency g-jitter in one time harmonic cycle in the absence of magnetic field.

Figure6. The development of the flow field caused by a single frequency g-jitter in one time harmonic cycle in the presence of magnetic field: (a) $t = 3.876$, $U_{\max} = 0.1603$
(b) $t = 3.927$, $U_{\max} = 0.5483$ (c) $t = 3.978$, $U_{\max} = 0.1603$ (d) $t = 4.029$, $U_{\max} = 0.5483$.

Figure7. The development of the concentration distribution caused by a single frequency g-jitter in of one time harmonic cycle in the presence of magnetic field: (a) $t = 3.876$ (b) $t = 3.927$ (c) $t = 3.978$ (d) $t = 4.029$. From left to right, $C_{\max} = 3.50$ reduced to $C = 1.04$, $\Delta C = 0.35$

Figure8. The development of (a) interface positions, (b) the temperature and (c) concentration distributions along the growth interface caused by a single frequency g-jitter in of one time harmonic cycle in the presence of magnetic field.

Figure9. The effects of the magnetic field on the velocity and concentration oscillation caused by a single frequency g-jitter at selected points in the melt near the growth front (a) $x=3.6$, $y=0.5$ (b) $x=3.6$, $y=0.5$ (c) $x=3.6$, $y=0.1$ and $x=3.6$, $y=1.3$.

Figure10. The effects of the magnetic field on the velocity and concentration oscillation caused by real g-jitter data at selected points in the melt near the growth front (a) $x=3.6$, $y=0.5$ (b) $x=3.6$, $y=0.5$ (c) $x=3.6$, $y=0.1$ and $x=3.6$, $y=1.3$.

Figure11. The development of (a) growth interface positions and (b) the concentration distributions along the growth interface caused by real g-jitter data without and with magnetic field at the selected time.

Figure12. The time variations of the concentration uniformity along the growth interface, which measured by $(C(t)_{\max} - C(t)_{\min})/C(t)_{\text{average}}$ with and without the applied magnetic field respectively.

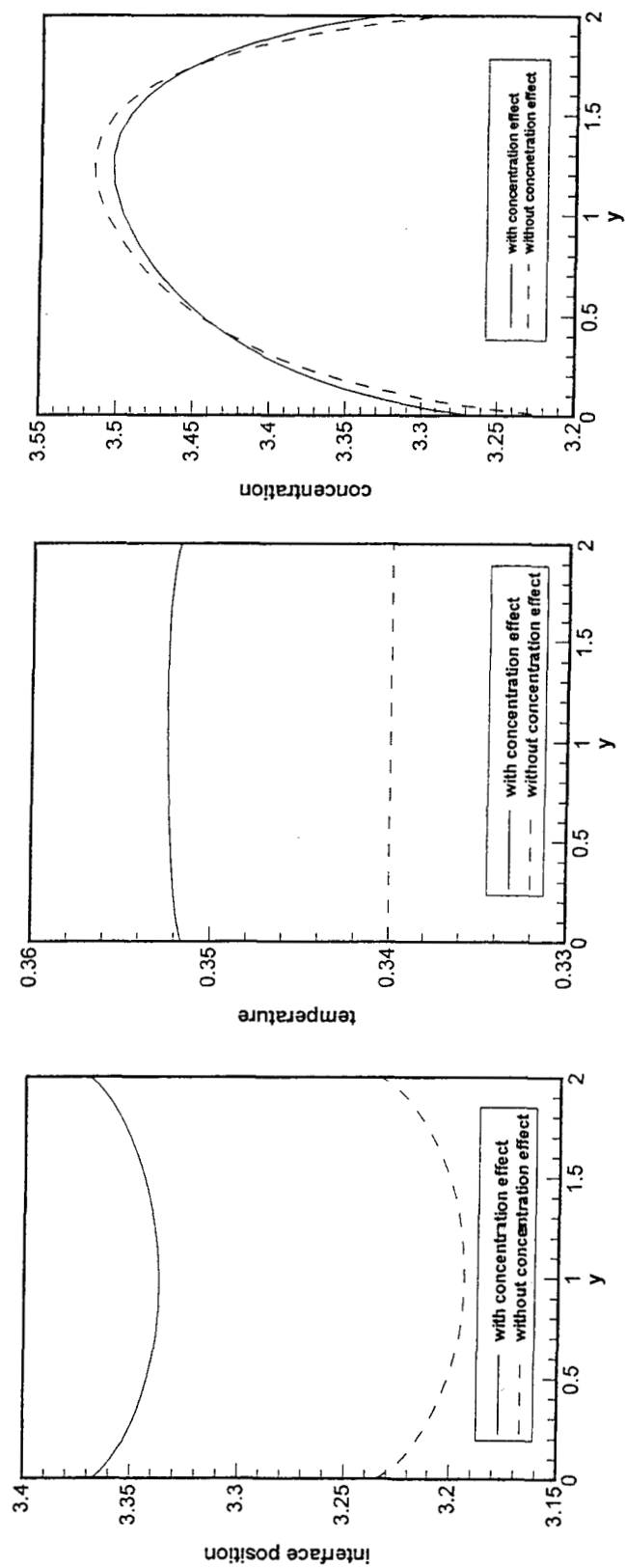


Figure 2(a)

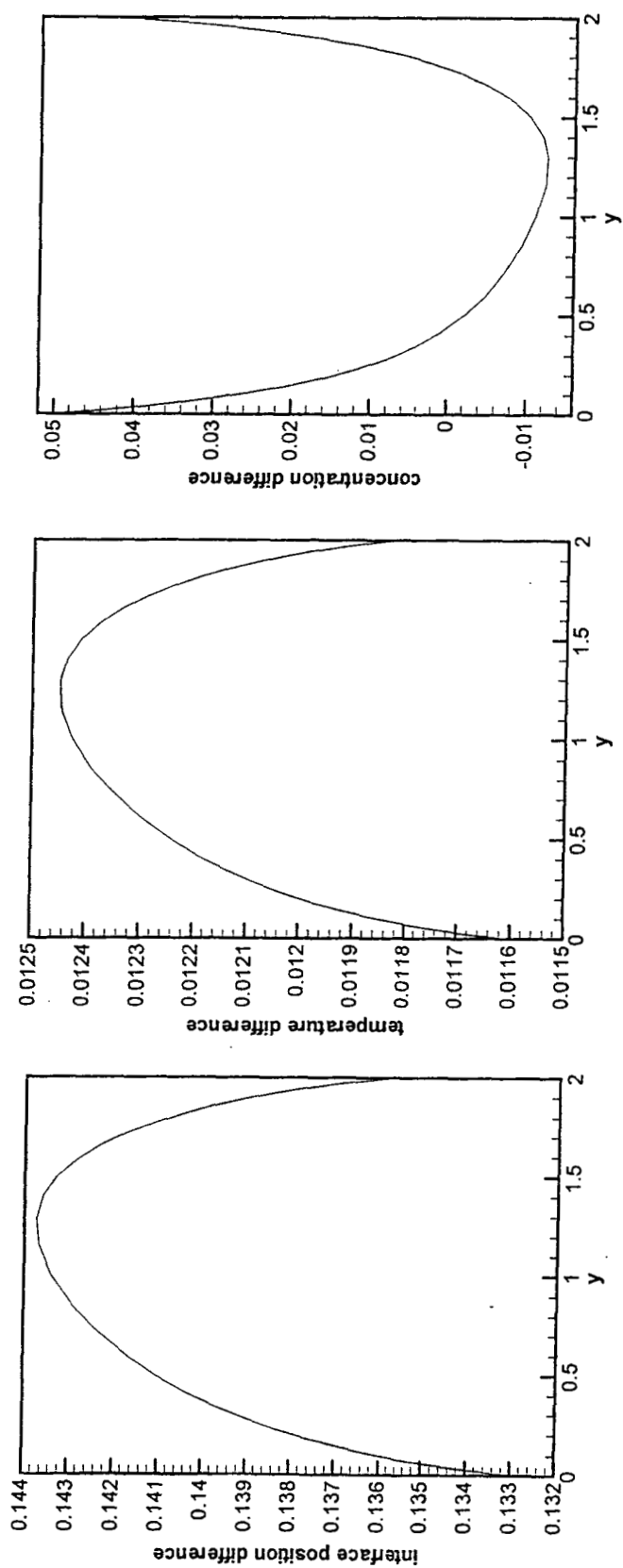
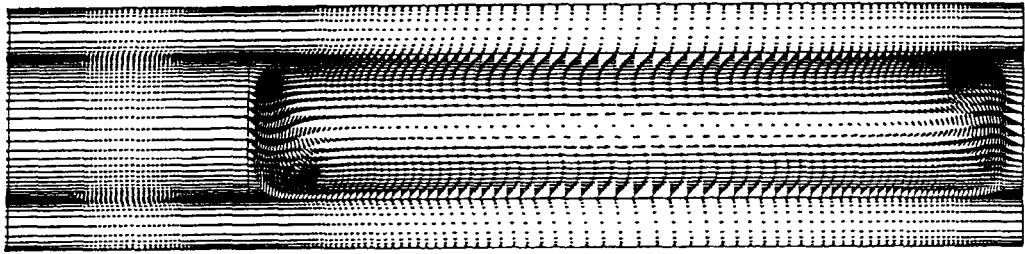
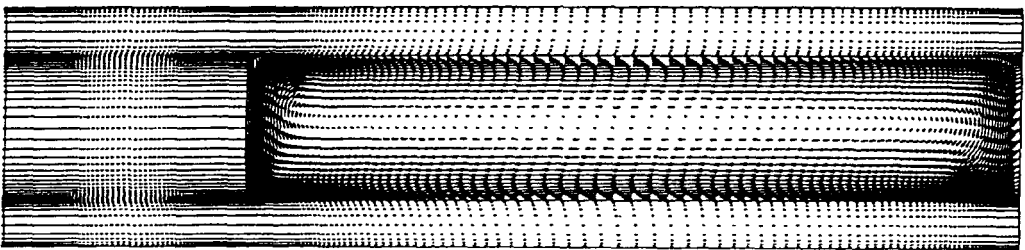


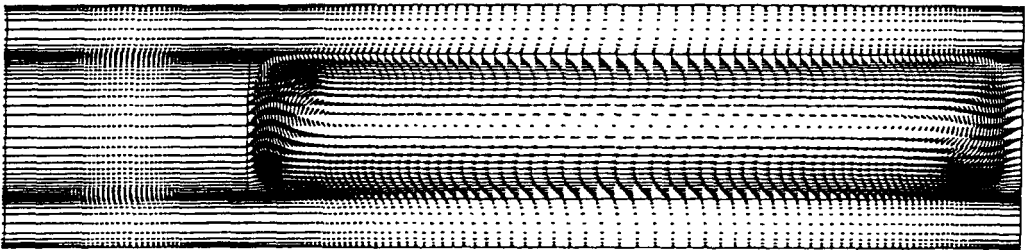
Figure 2(b)



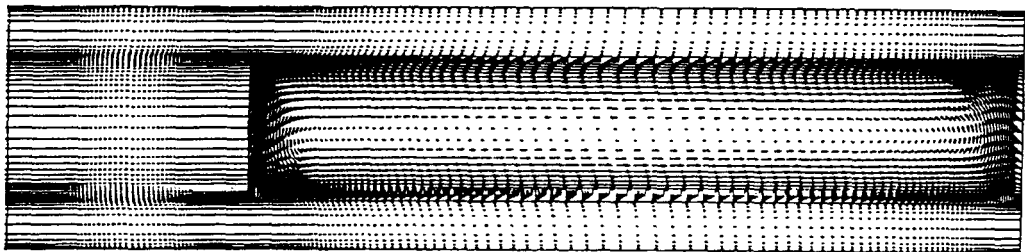
(a)



(b)

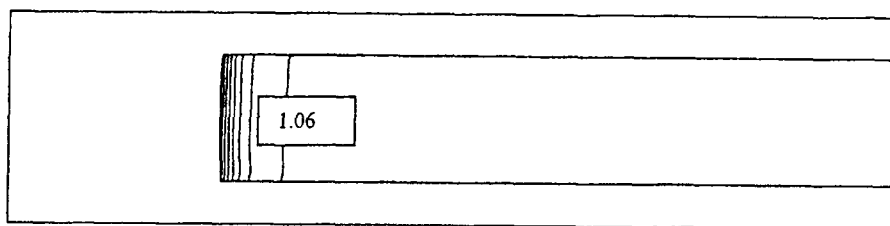


(c)

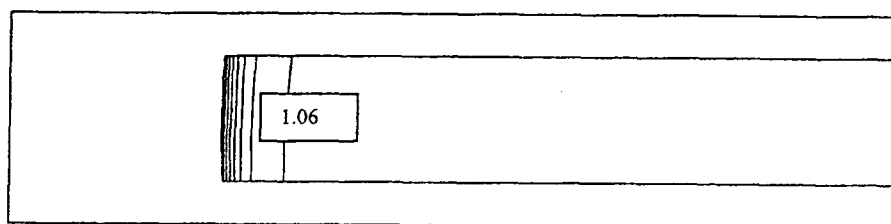


(d)

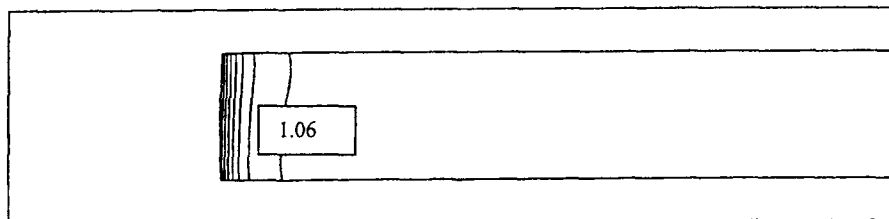
Figure 3



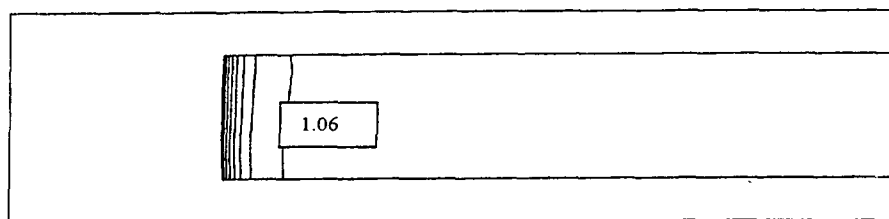
(a)



(b)



(c)



(d)

Figure 4

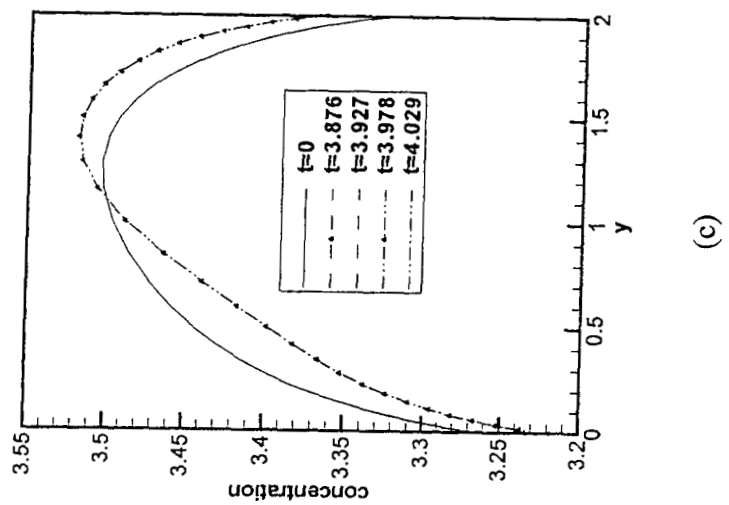
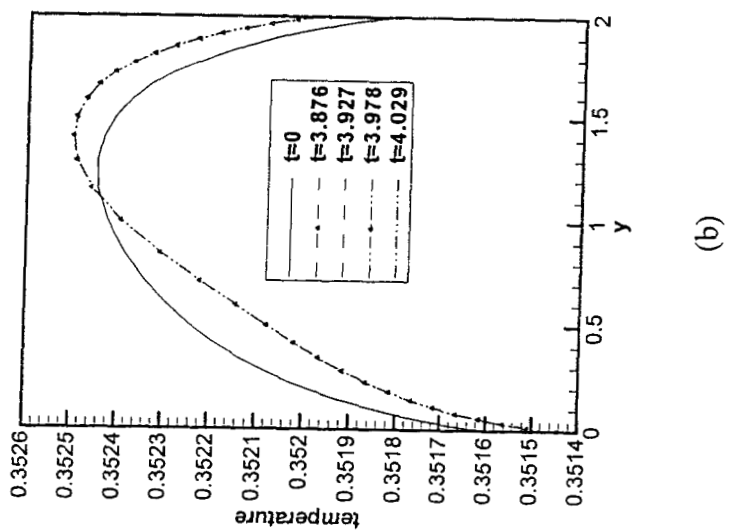
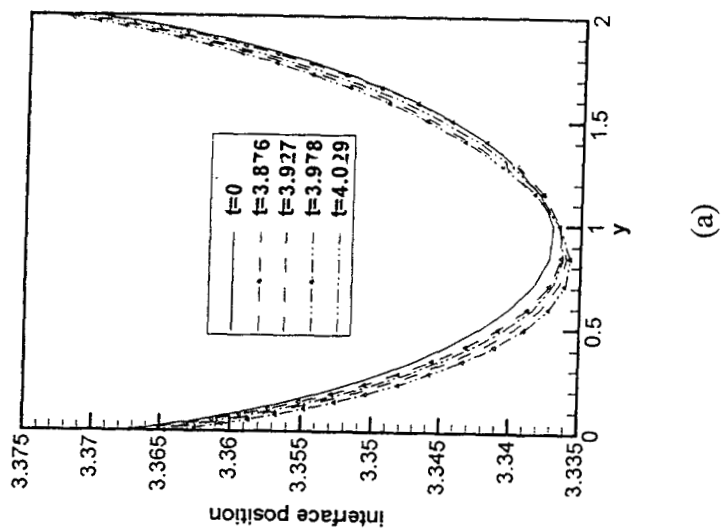
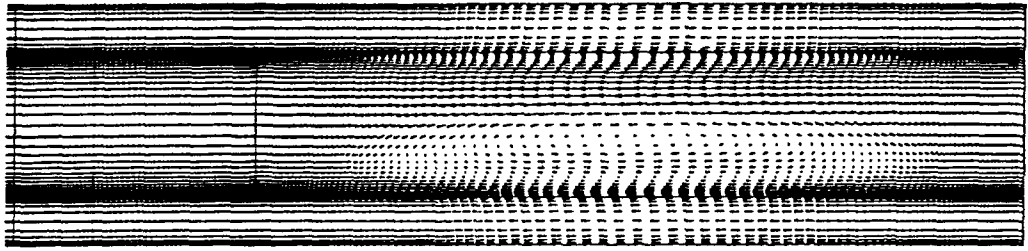
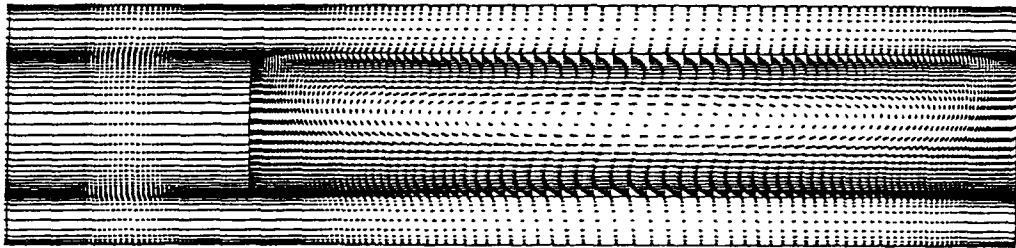


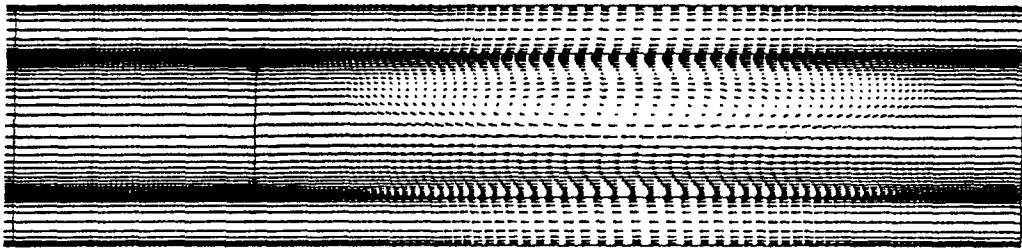
Figure 5



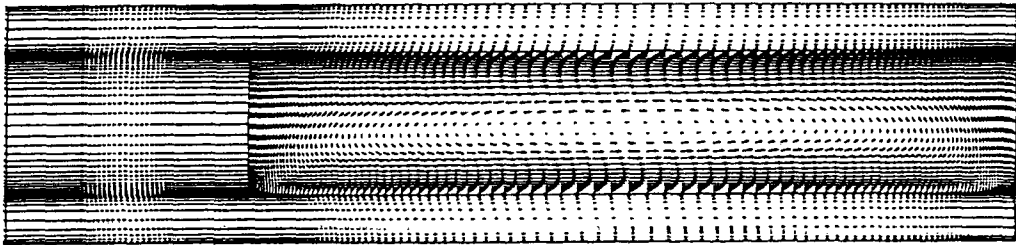
(a)



(b)

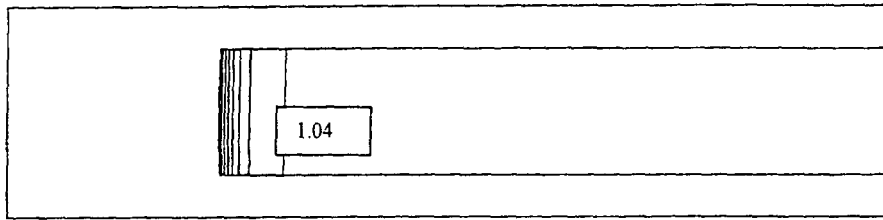


(c)

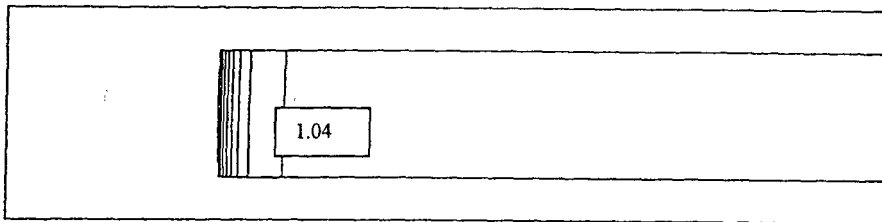


(d)

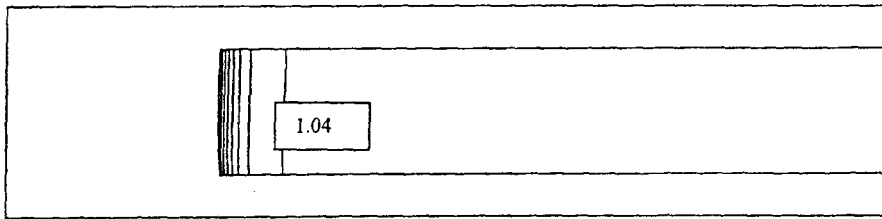
Figure 6



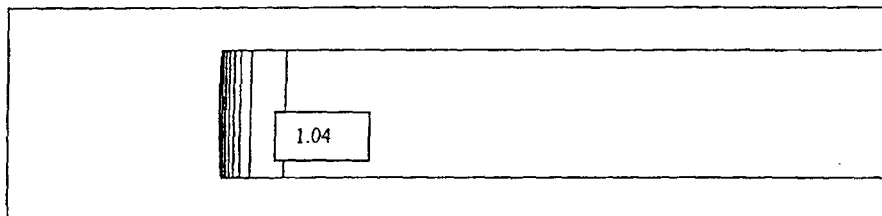
(a)



(b)

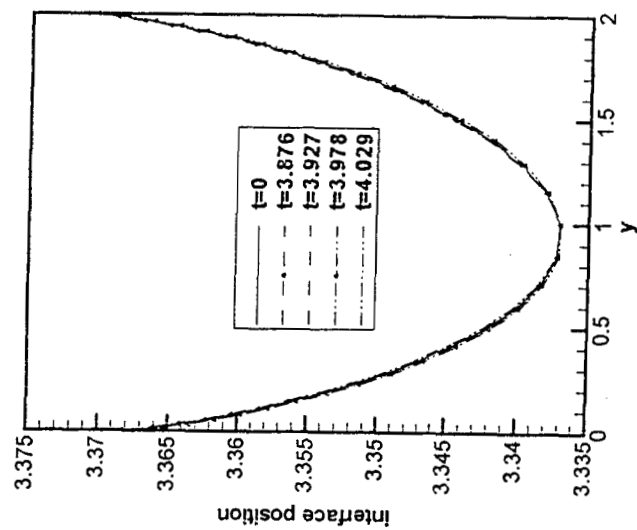


(c)

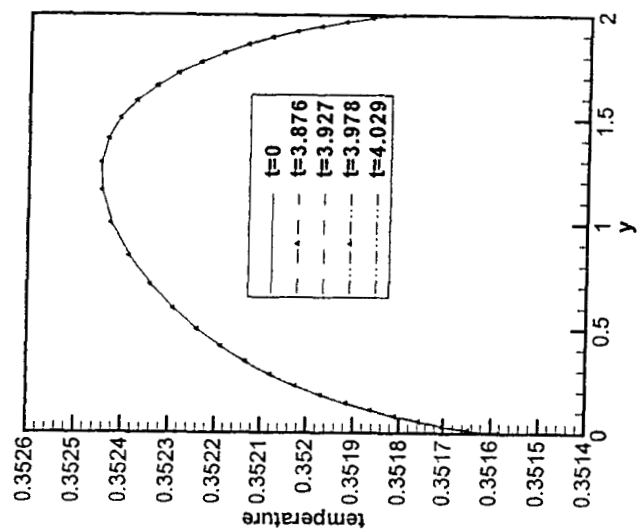


(d)

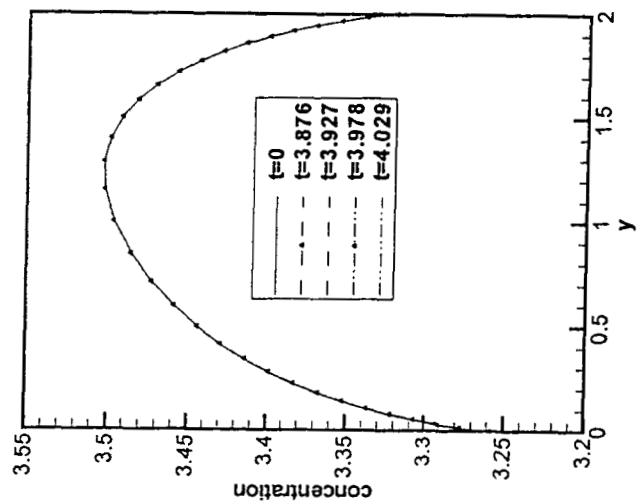
Figure 7



(a)

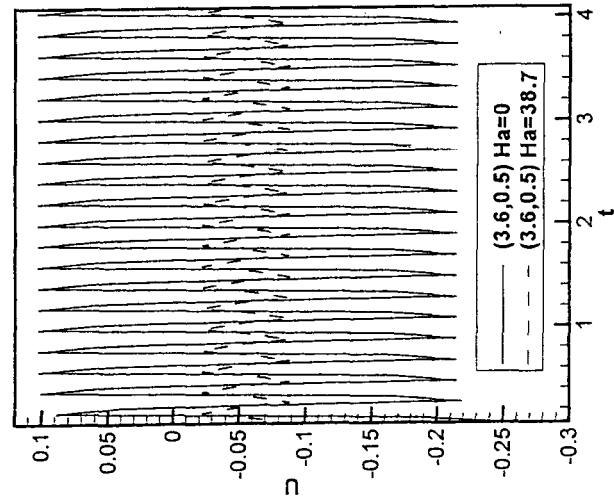


(b)

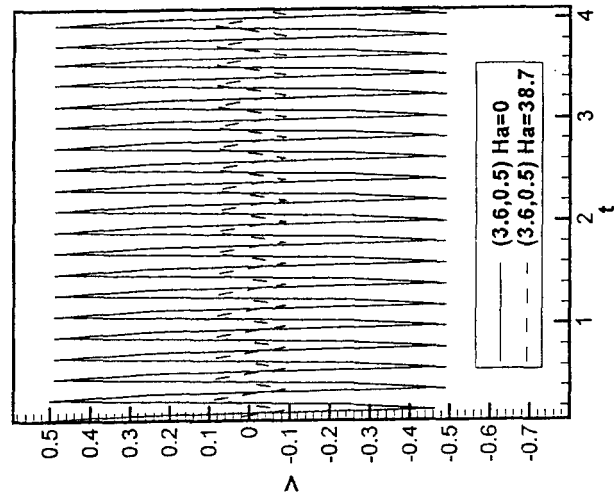


(c)

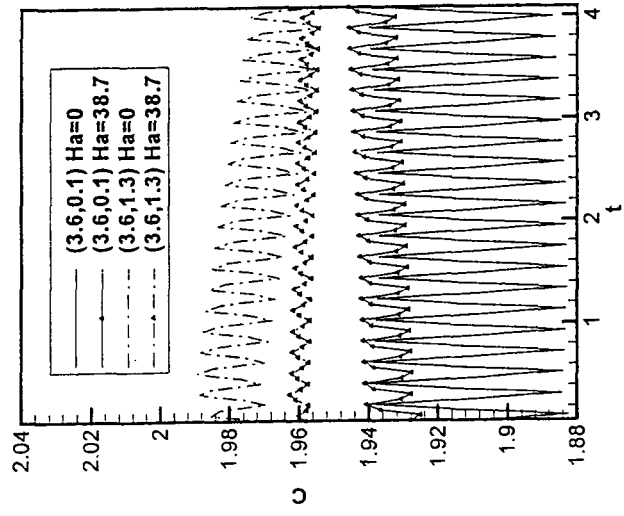
Figure 8



(a)



(b)



(c)

Figure 9

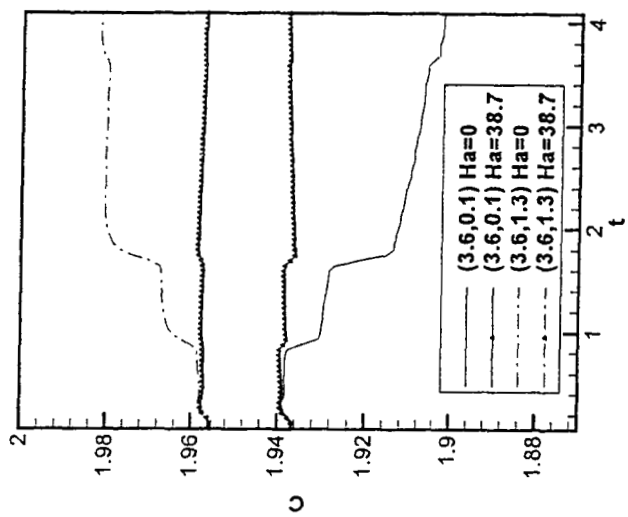
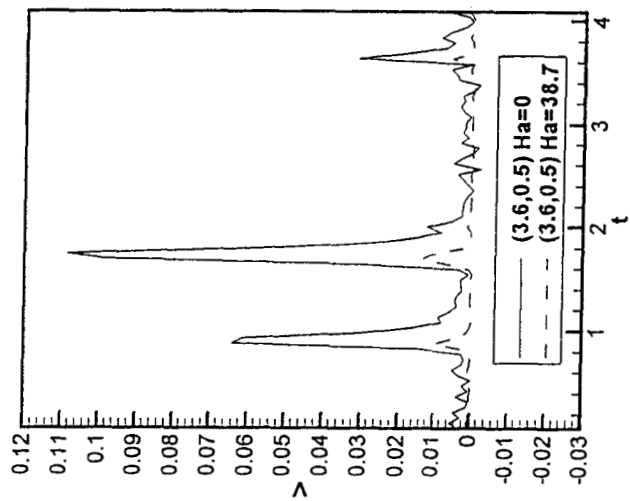
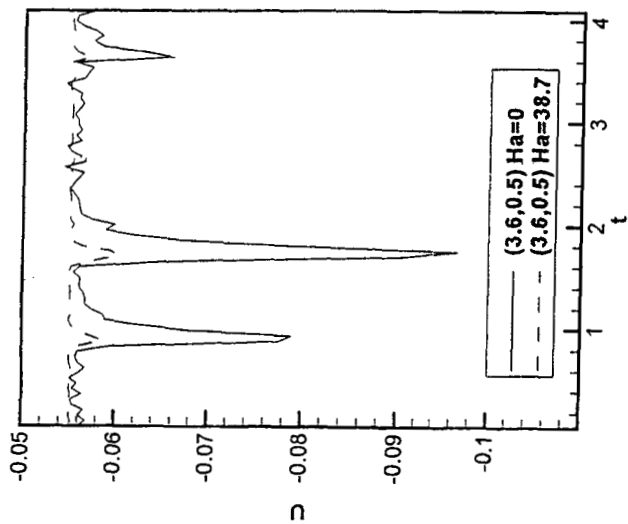
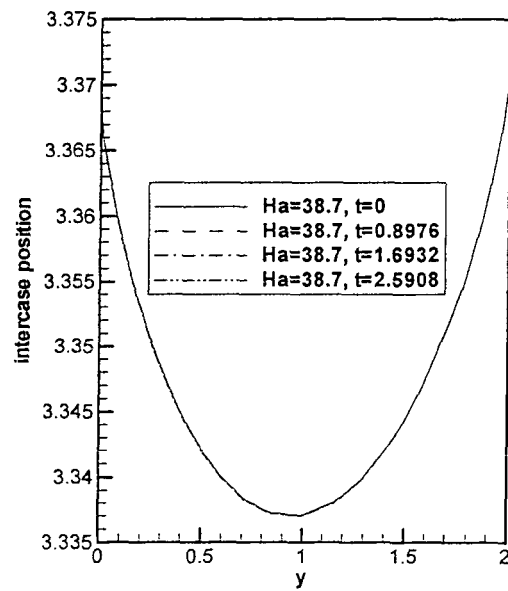
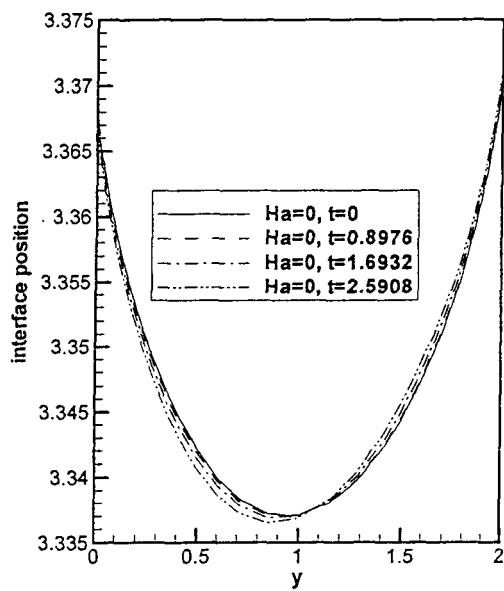
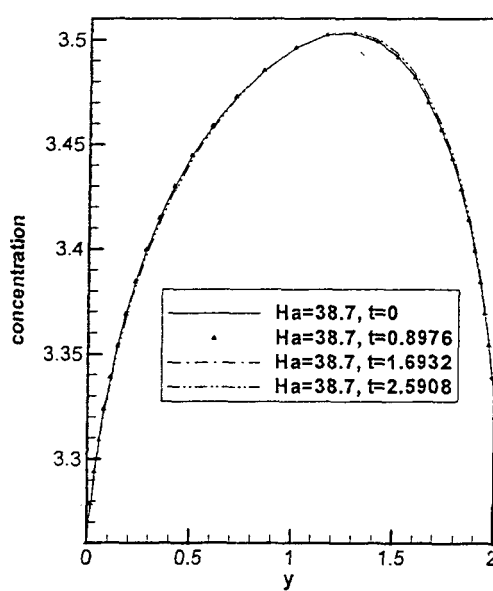
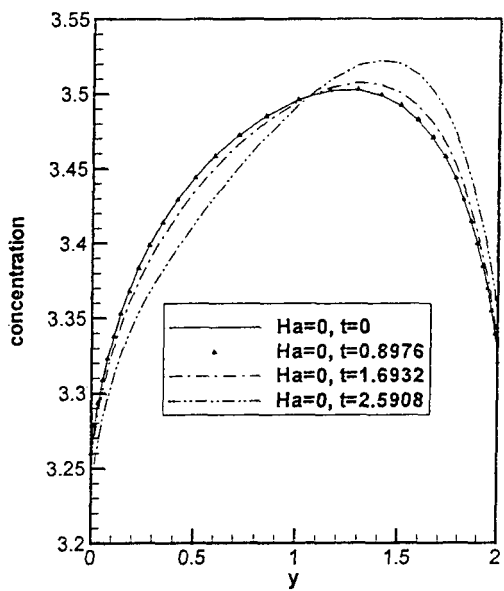


Figure 10



(a)



(b)

Figure 11

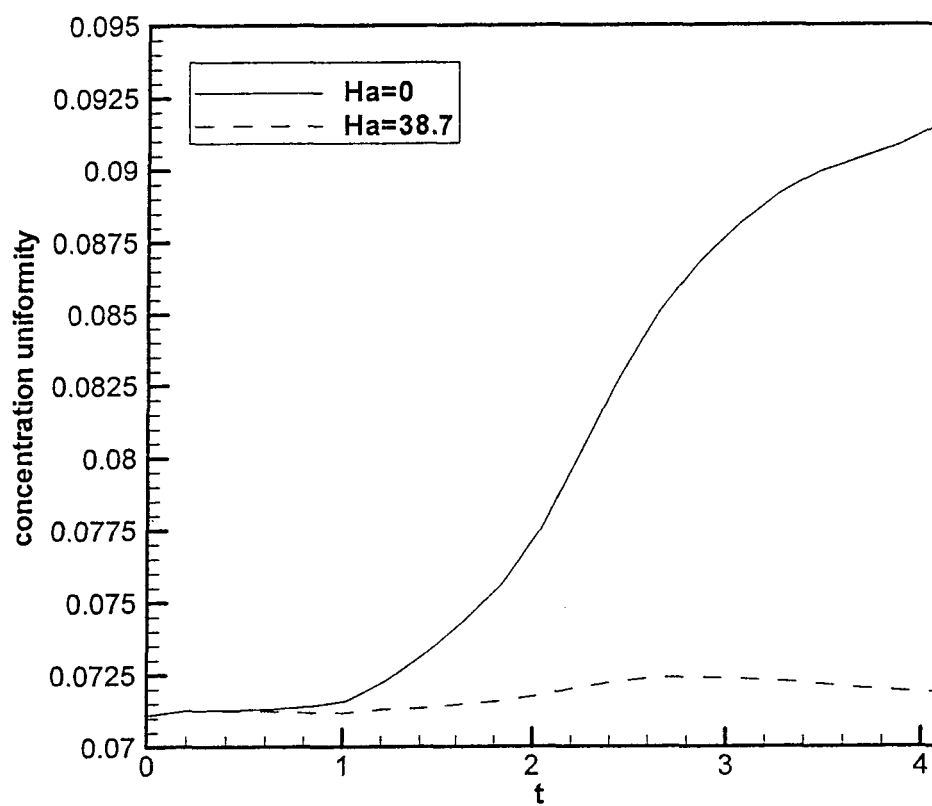


Figure 12